Biological and medical applications of low-intensity ultrasound

Spiros Kotopoulis, Anthony Delalande, Chantal Pichon, Michiel Postema

7

Biological and medical applications of low-intensity ultrasound*

Spiros Kotopoulis[1,4], Anthony Delalande[2,4], Chantal Pichon[3], Michiel Postema[4]

[1]National Centre for Ultrasound in Gastroenterology, Haukeland University Hospital, Bergen, Norway
[2]Department of Haematology, Haukeland University Hospital, Bergen, Norway
[3]Centre de Biophysique moléculaire, CNRS, Orléans, France
[4] Department of Physics and Technology, University of Bergen, Bergen, Norway

Abstract

Ultrasound is currently used for a vast range of non-destructive testing, evaluation and diagnostics in both industry and medicine. Here we present some results indicating possible uses of low-intensity ultrasound in biology, specifically in the control of blue-green algal growth, and in the medical field to facilitate targeted increased drug uptake. Our results showed that pulsed ultrasound well within the clinical diagnostic range could be used to control algal blooms by bursting the gas-vesicles, forcing the algae to sink. Using continuous wave ultrasound we showed that it is possible to force ultrasound contrast agents to form clusters at a quarter-wavelength of the sonication frequency. Furthermore, using low-intensity pulsed ultrasound we showed that it was possible to force an ultrasound contrast agent, coated with a fluorescent dye, into cancerous cells.

Ultrasound-induced cracking of *Anabaena sphaerica*

Introduction

Algae are aquatic, eukaryotic, photosynthetic organisms, ranging in size from single-celled forms to large kelps. Algae are classified separately from plants since they lack true roots, stems, leaves and embryos. Blue-green algae are known to cause many health hazards to humans including skin rashes, gastrointestinal, respiratory [1], allergic reactions [2] and liver cancer [3]. In addition, blue-green algae may have implications on aquatic and semi-aquatic animals [4].

Eutrophication is the increase in chemical nutrients within the ecosystem, causing blooms of algae and plant life and the subsequent decomposition of blue-green algae by bacteria; an oxygen-consuming process [5]. When billions of such bacterial cells die simultaneously after a bloom, the water becomes oxygen-depleted, killing off oxygen-dependent organisms [6]. The main factors that influence algae growth are temperature and light [7, 8]. At low temperatures and low light conditions, the algae do not photosynthesise and therefore do not bloom. Blue-green algae strands contain nitrogen-producing cells (heterocysts) shown in Fig. 1, these cells have a diameter between 5 and 7 μm. These store the necessary nitrogen and distribute it to other cells [9].

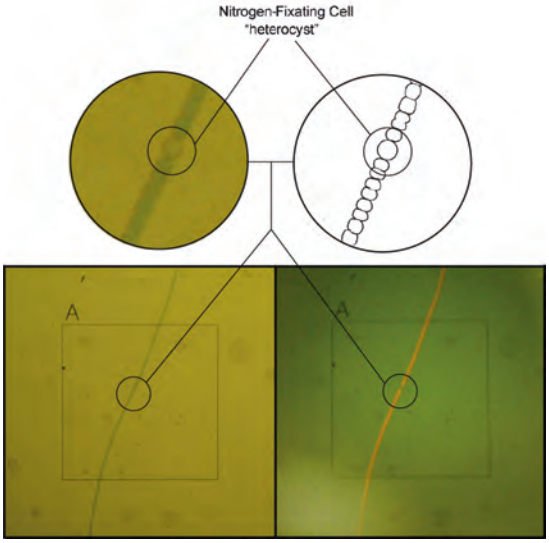

Figure 1 - Nitrogen-fixating body in *Anabaena sphaerica* algae. Under fluorescent light the body does not illuminate red, proving there is no chlorophyll in the body. Each frame corresponds to 565×565 $(\mu m)^2$.

It is hypothesised that if the membranes of the gas vesicles are disrupted by means of ultrasound, the gas may be released analogous to sonic cracking [10], causing the gas to diffuse and have no means to replenish, thus forcing the strands to sink. At the lakebed, illumination is lower, thus reducing blue-green algae growth. This is a desirable ecological effect, because of resulting suppressed release of toxins into the water.

There are chemical methods to control certain species of blue-green algae but these have side effects such as promotion and growth of other species of algae [11] whilst also affecting aquatic life in fresh water ponds and lakes. Therefore, ultrasonic algae control has been under investigation [12-17]. In [12-17] ultrasonic sonication of different species of algae led to a decrease in algae concentration in the frequency range 20 kHz–1.7 MHz, which is in contrast with [18], where ultrasound was observed to strengthen the cell membranes of red algae. In these studies the exact acoustic conditions have not been specified other than the frequency and power input. Hence, from the acoustics point of view, they are not repeatable. More importantly, the mechanism causing algae eradication or membrane disruption had not been investigated.

Most commercially available equipment works in the lower ultrasonic range [19]. There have been speculations about the physical mechanism behind the algae eradication, specifically about the role of cavitation. In this study, the effectiveness of ultrasonic sonication in the clinical diagnostic range on *Anabaena sphaerica* was investigated.

In this chapter, acoustic fields in the lower clinical diagnostic range were used, taking into account the MI and NURC guidelines.

Materials and Methods

To investigate the effect of diagnostic ultrasound on blue-green algae eradication, three ultrasound transducers were used. A 200-kHz, single element transducer containing a PIC155 piezo crystal (PI Ceramics, Lederhose, Germany), a PA188 (Precision Acoustics Ltd., Dorchester, UK) 1-MHz, single element transducer, and a 2.2-MHz, single element transducer containing a Pz37 piezo crystal (Ferroperm Piezoceramics A/S, Kvistgård, Denmark). The focal distance of the 2.2-MHz transducer was 73mm. The design of two transducers is shown in Fig. 2. The transducers were subjected to 260-Vpp sinusoidal pulses at a 11.8-kHz pulse repetition rate transmitted by a V1.0 pulser-receiver (Sonemat, Coventry, UK). Low acoustic amplitudes were used in order to comply with MI<0.3 [20]. The acoustic amplitudes were measured in a separate water tank in the acoustic foci of the transducers with a 0.2-mm needle hydrophone (Precision Acoustics Ltd.) connected to a TDS 420A digitising oscilloscope (Tektronix Inc, Beaverton). The peak-negative acoustic pressures were 40 kPa for the 1-MHz transducer and 68 kPa for the 2.2-MHz transducer, *i.e.*, MI$\ll$0.1.

The blue-green algae used were of the Anabaena species. The Anabaena were obtained from a natural lake and cultured in 2 L of Jaworski's medium [21] at room temperature near a South-facing window in an Erlenmeyer flask for 11 days. Prior to

adding the blue-green algae the Jaworski's medium was put in a Swirtlock 2000 autoclave (Astell Scientific, Kent, UK) at 15-lb pressure for 15 minutes.

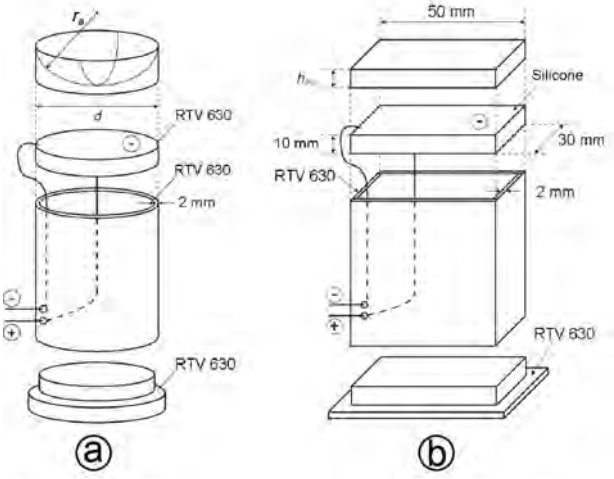

Figure 2 - (a) 2.2-MHz ultrasound transducer with $\boldsymbol{d = 1}$" diameter and $\boldsymbol{r_a = 35}$ mm acoustic lens. (b) 200-kHz ultrasound transducer with $\boldsymbol{h_{PG} = 10}$ mm matching layer.

Brightness measurements

To measure the time-dependent change in brightness of water containing blue-green algae, the culture was split equally into four 250-mL Perspex beakers: one beaker for each transducer and one control beaker. The transducers were inserted separately in each beaker with the acoustic focus within the sample. Each transducer was turned on for 1 hour. The experimental setup is shown in Fig. 3. A digital photograph of the solution was taken every five minutes using an EOS 350D digital photo camera (Canon Inc, Tokyo, Japan). The lighting and exposure settings were controlled and maintained throughout the sonication. Full manual settings were used: 100 ISO, shutter speed of 1/50 s, f 3.50, focal length of 18mm, no flash, centre weighted metering mode, custom white balance with a B4,0 shift. The digital photographs were converted to 8-bit grey scale. On the photographs of the sonicated solution and control solution, a square area of 160×160 pixels (A1 and B1) in the middle of the beaker, and an area of 160×50 pixels (A2 and B2), at the base of the beaker, was selected, whose average grey-scale depth was calculated using Matlab® (TheMathworks™, Natick, MA). The change in shade between the first image, taken just before sonication and each sequential image after sonication was calculated and graphed for all 18 sonicated and control samples. A white sheet was placed behind the beakers to maintain a constant background. The grey scale of the sheet was also measured and used to calibrate the results. In total, 575 measurements were analysed from 122 photographs.

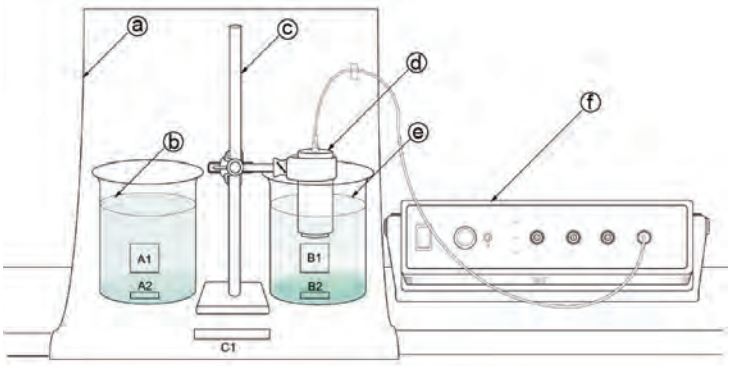

Figure 3 – Experimental setup: (a) white paper sheet; (b) control sample; (c) clamp stand; (d) transducer; (e) sonicated sample; (f) pulser-receiver. Areas A1-B2 represent brightness measurement areas, C1 represents the calibration area.

Viability measurements

Every 10 minutes, a 20-μL sample was taken from the sonicated solution. Samples were put on a test slide and observed through a CHA microscope (Olympus Corporation, Tokyo, Japan) with an MPlan 10×0.30 NA objective lens (Olympus Corporation) *cf.* Fig. 4. Digital photographs were captured from the microscope's eyepiece using an FE-230 digital camera (Olympus Corporation). Automatic settings were used with Super Macro mode and a −1.0 exposure adjustment. From these digital images deterioration in chlorophyll activity and cell damage was determined. To investigate the effect of ultrasound on the viability of the cells, fluorescent light was used. When fluorescent light is projected onto chlorophyll, it is absorbed and re-emitted as a red glow. The red glow denotes that the chlorophyll is still active and can photosynthesise, thus the blue-green algae strands are still alive.

Fluorescent light was used as the method to check the viability of the chlorophyll, since it is a standardised and accepted method in detecting chlorophyll activity in plants [83, 138]. Fluorescent light was projected onto these samples for no more than 10 seconds in order to capture the digital image. It may assume that there are no disadvantageous effects of the fluorescent light on the blue-green algae [65, 95].

The samples were discarded after being exposed to fluorescent light. Three trials of each frequency were performed. One hundred and thirty-one photographs were taken of the microscopic cell structure.

Post-sonication growth measurements

To measure the effect of ultrasound on blue-green algae growth post-sonication, twenty-four 1-mL samples were removed from three solutions that had been subjected to 1-hour sonication with 200-kHz, 1.0-MHz and 2.2-MHz ultrasound and put into a

culture tray with 96 compartments. Twenty-four control samples were taken. The culture tray was left in sunlight for 30 days. The grey scale value was measured for each compartment.

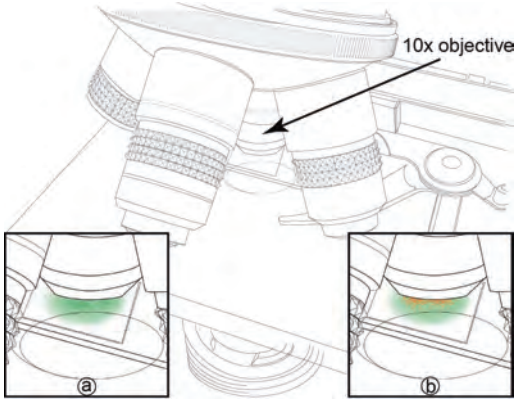

Figure 4 - Schematic showing use of the fluorescence microscope. A 10× objective lens was used. (a) Blue-green algae under tungsten lighting; (b) Blue-green algae under fluorescent lighting.

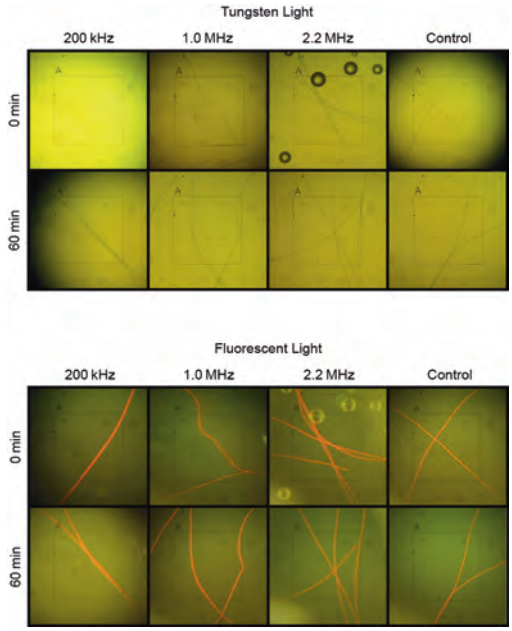

Figure 5 – Microscopic image sequence showing the effect of 200 kHz–2.2 MHz ultrasound on the floating bodies of blue-green algae. Each frame corresponds to 565×565 $(\mu m)^2$.

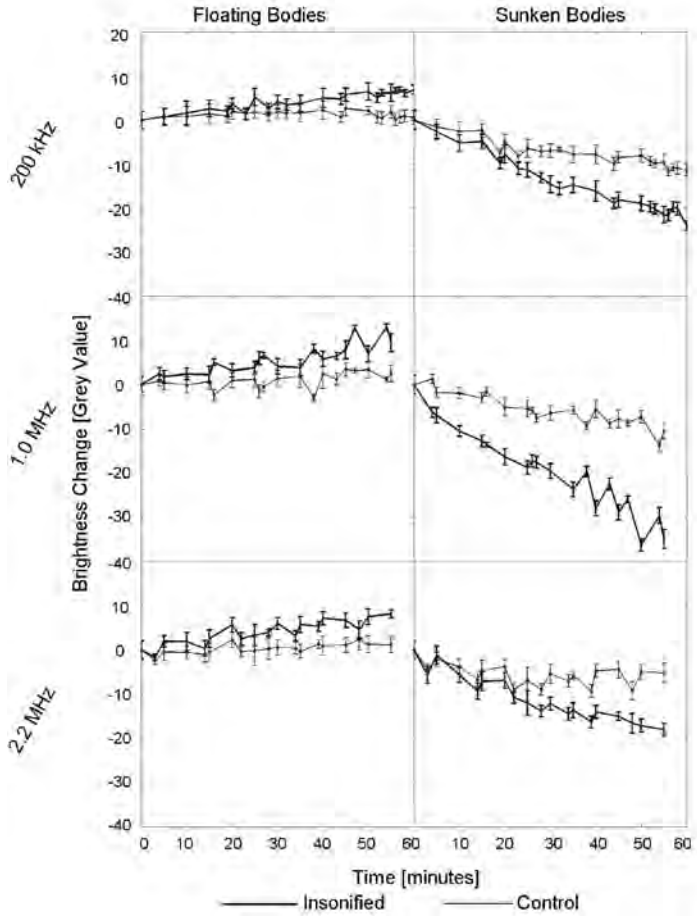

Figure 6 - Water brightness as a function of ultrasonic exposure time for samples containing floating blue-green algae or sunken blue-green algae.

Results and discussion

Figure 5 shows the microscopic effect of ultrasound on floating bodies in the blue-green algae solution. From 0 minutes to 60 minutes of sonication, no change was seen in the physical structure of the blue-green algae for all three frequencies. Fluorescent illumination showed that the ultrasound had no effect on the chlorophyll activity for the all frequencies tested. The active chlorophyll shows that the blue-green algae strands are still alive and able to photosynthesise after 60 minutes sonication. This indicates

that the ultrasound transmitted does not affect the chlorophyll in the cells.

However, Fig. 6 shows that at all frequencies, for the floating bodies, the sonicated samples showed greater brightness than the control samples. For the sunken bodies, all sonicated samples showed reduced clarity when compared to the control samples. Thus, the ultrasound has caused the algae to sink. For example, after 60 minutes, the beakers subjected to 200-kHz sonication were 92±12% brighter than the control samples, contrasted by the beaker bottoms, which were 53±27% darker than the control samples.

Clearly, the blue-green algae that were floating in the beaker dropped to the bottom at a faster rate than the control sample. This has been attributed to the disruption of the floating bodies by the ultrasound. This is supported by Fig. 7, which shows that the sunken bodies still have active chlorophyll but less dense kelps were found.

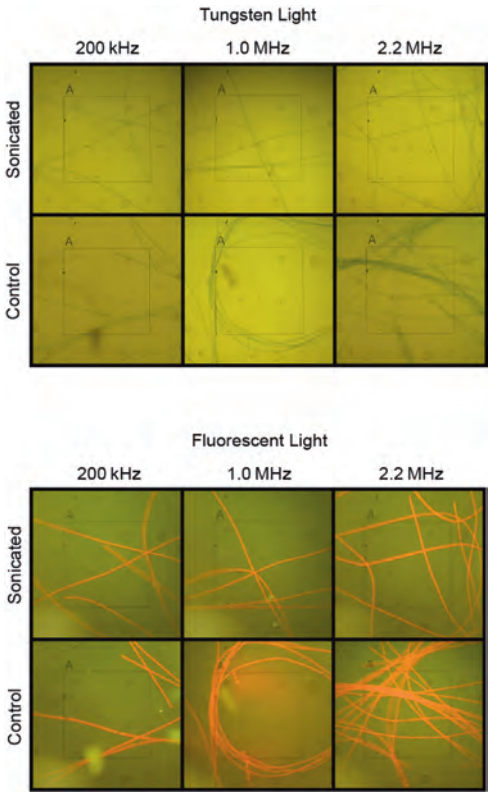

Figure 7 – Microscopic image sequence showing the effect of 200 kHz–2.2 MHz ultrasound on sunken blue-green algae. Each frame corresponds to 565×565 $(\mu m)^2$.

Figure 8 shows the viability of the culture 30 days after sonication in terms of sample brightness. At 200 kHz, 1.0 MHz, and 2.2 MHz, the samples were 39±14%, 45±17%, and 46±17% brighter than the control samples, respectively. All samples were significantly brighter than the control samples, even at the lower boundaries of the standard deviation. Thus, these results support the hypothesis that the blue-green algae that have sunk are less capable of multiplying. Hence, sonication may prevent blue-green algae bloom.

The results can be interpreted as follows. When a gas vesicle is subjected to an ultrasound pulse it expands during the rarefaction phase [22]. If the acoustic amplitude is sufficiently high, the encapsulating membrane cannot withhold the bubble from further expanding, resulting in its rupture. This phenomenon is similar to the sonic cracking of micrometre-sized membrane-encapsulated bubbles observed in [10]. Sonic cracking exclusively occurs during the expansion phase of a bubble [23].

The resonance frequency f_0 of a an encapsulated microbubble is given by [24]:

$$f_0 = \frac{1}{2\pi}\sqrt{\left(\frac{3\Gamma}{{R_0}^2\rho}\right)\left(p_0 + \frac{2\sigma}{R_0} + \frac{2\chi}{R_0}\right) - \left(\frac{2\sigma + 6\chi}{{R_0}^3\rho}\right)}, \quad (1)$$

where p_0 is the ambient pressure, R_0 is the bubble radius, Γ is the polytropic exponent of the gas, ρ is the liquid density, σ is the surface tension, and χ is the elasticity of the encapsulation [110]. Using $p_0 = 1.013\times10^5$ Pa, $R_0 = 3\,\mu$m, $\Gamma = 1.4$, ρ is 998 kg m^{-1}, $\sigma = 0.072$ N m^{-1}, and assuming that the membrane elasticity is similar to that of a lipid encapsulation, $\chi = 0.044$ N m^{-1} [25], it can be estimated $f_0 \approx 1$ MHz for Anabaena cells used in these experiments. Since the greatest change in clarity was seen at this particular frequency, it can safely be stated that ultrasound sonication close to gas vesicle resonance frequency leads to a more effective eradication.

The quick decrease in live blue-green algae is similar to that in previous studies [12-17]. It can be assumed that the correlation between (high) frequency and algae eradication in these studies is related to the ultrasound proximity to gas vesicle resonance as well.

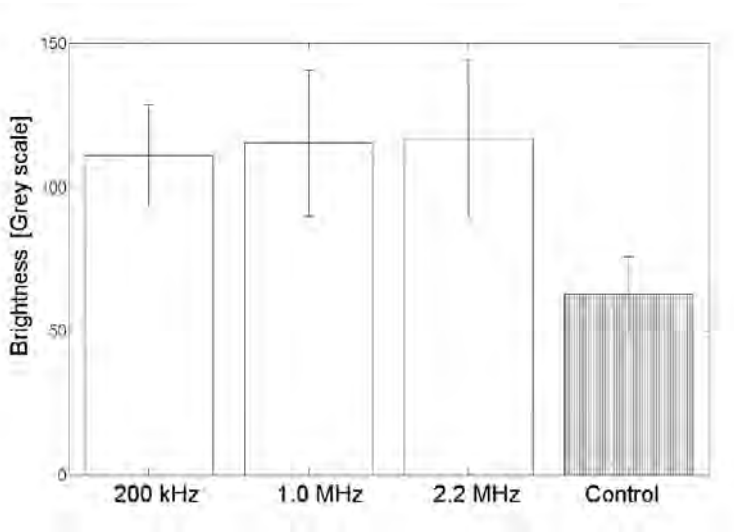

Figure 8 – Water clarity 30 days after sonication.

According to the NURC Rules and Procedures [20], the maximum acoustic pressure to which mammals can be exposed is 708 Pa at frequencies up to 250 kHz.

The transducers used had acoustic pressures of 40 kPa and 68 kPa at driving frequencies 1.0 MHz and 2.2 MHz, respectively. These pressures surpass the NURC Rules and Procedures by over 35 dB.

Conclusion

At any ultrasonic frequency studied, blue-green algae were forced to sink. This supports the hypothesis that the gas vesicles release their gas under ultrasound sonication in the clinical diagnostic range. As supported by previous studies, under identical pulse length and pulse repetition, eradication is most effective close to gas vesicle resonance, at a driving frequency of roughly 1 MHz.

Although the acoustic fields used to eradicate blue-green algae are safe in terms of mechanical index, the acoustic pressures surpass the NURC Rules and Procedures by over 35 dB. Therefore, caution should be taken when using these techniques in a surrounding where aquatic or semi-aquatic animals are present.

Microfoam formation in capillaries

Introduction

Ultrasound contrast agents are used in diagnostic imaging. They consist of microscopically small bubbles containing slowly diffusing gas encapsulated by biodegradable shells. When inserted in the blood stream, these bubbles oscillate upon ultrasonic sonication, thereby creating detectable ultrasound themselves. A brief overview of the most common ultrasound contrast agents has been presented in [26]. It follows that albumin and lipids are currently the most common bubble encapsulation materials. Because of the proven feasibility to attach therapeutic compounds to albumin and lipids, therapeutic application of contrast agents have become of interest [1, 27-29]. It is desirable that the therapeutic load of any such contrast agent is released close to the vessel wall. Therefore, pushing bubbles towards boundaries by means of primary radiation forces has been studied [30].

Both primary and secondary radiation forces resulting from oscillating bubbles, may cause the repulsion or mutual attraction, and eventual collision and coalescence, of contrast agent bubbles. This phenomenon has been less studied.

From the therapeutic point of view, the formation of bubble clusters may be of interest. If the clusters behave as one entity, *i.e.*, one mega-bubble, its ultrasonic manipulation towards a boundary is fairly straightforward and quick. If the clusters can be forced to accumulate to a microfoam, entire vessels might be blocked on purpose using an ultrasound contrast agent and a sound source.

In this chapter, how ultrasound contrast agent clusters are formed and what happens to the clusters if sonication is continued is analysed. Furthermore, high-speed camera footage of microbubble clustering phenomena is shown and the therapeutic consequences of these findings is discussed.

Theory

A brief overview of theory on radiation forces and ultrasound contrast agent has been given in [109]. Bubble translation in the direction of the sound field is caused by a primary radiation force resulting from a pressure gradient across the bubble surface. The translation is maximal during the contraction phase. The velocity v of a bubble in a steady fluid subjected to an ultrasound field can be calculated using [31]:

$$F_{\mathrm{r}} + F_{\mathrm{d}} - \frac{\mathrm{d}(mv)}{\mathrm{d}t} \approx 0, \tag{2}$$

where F_r is the primary radiation force, F_d is the drag force, $m = \frac{2}{3}\pi\rho R_0^3$ is the added mass of the translating bubble, equivalent to half the mass of the displaced surrounding fluid, in which R_0 is the equilibrium bubble radius and ρ is the density of the surrounding fluid. Averaging over one acoustic cycle, the primary radiation force is given by [31-33]:

$$F_{\mathrm{r}} = \frac{p_a^2 R_0}{\rho c f} \frac{\delta\left(\frac{f_0}{f}\right)}{\left[\left(\frac{f_0}{f}\right)^2 - 1\right]^2 + \left[\delta \frac{f_0}{f}\right]^2}; \tag{3}$$

where c is the speed of sound, p_{a} is the peak rarefactional acoustic pressure, δ is the dimensionless total damping coefficient [34], f is the driving frequency, and f_0 is the bubble resonance frequency [34]. The drag force is given by [33, 34]:

$$F_{\mathrm{d}} = -\frac{\pi\eta}{4} C_{\mathrm{d}}\,\mathrm{Re}\,R_0\,v(t), \tag{4}$$

where η is the shear (dynamic) viscosity of the fluid, $Re = \frac{2\rho R_0}{\eta}|v(t)|$ is the Reynolds number, and

$$C_{\mathrm{d}} = -\frac{24}{\mathrm{Re}}(1 + 0.15\,\mathrm{Re}^{0.687}), \tag{5}$$

is the drag coefficient of a contaminated system [35], such as a contrast agent.

Combining Eqns. 2 – 4 and integrating over $\mathrm{d}t$ gives the following expression for the average velocity of a bubble:

$$v = \frac{4p_{\mathrm{a}}^2}{\rho\, c\, f\, \eta\, C_{\mathrm{d}}\,\mathrm{Re}} \frac{\delta\left(\frac{f_0}{f}\right)}{\left[\left(\frac{f_0}{f}\right)^2 - 1\right]^2 + \left[\delta\left(\frac{f_0}{f}\right)\right]^2} \left[1 - e^{\left(-\frac{3\,\eta\, C_{\mathrm{d}}\,\mathrm{Re}}{8\,\rho\, R_0^2} t\right)}\right]. \tag{6}$$

Secondary radiation forces, resulting from oscillating bubbles under sonication, may cause the mutual attraction and subsequent coalescence of contrast microbubbles. Two bubbles that oscillate in phase approach each other, whereas two bubbles that oscillate out of phase recede from each other [22, 36]. At low acoustic amplitudes, the phase angle difference φ between excursion of the oscillating bubble and the incident sound field is given by [22, 32, 36]:

$$\phi = \pi + \arctan\left(\frac{\delta\left(\frac{f}{f_0}\right)}{1 - \left(\frac{f}{f_0}\right)^2}\right). \tag{7}$$

The presence of an encapsulating shell increases the damping coefficient by a term δ_s [37].

$$\delta_s = \frac{S_f}{2\pi m f_0}, \tag{8}$$

and increases the squared resonance frequency f_0^2 by a term f_s^2 [37]

$$f_s^2 = \frac{\chi}{2\pi R_0^3 \rho}; \tag{9}$$

where S_f is the shell friction [37] and χ is the shell stiffness parameter [22, 37]

$$\chi = \frac{E\epsilon}{1-v}; \tag{10}$$

where E is Young's modulus, ϵ is the shell thickness, and v is Poisson's ratio.

The mean approach velocity v of two identical bubbles is given by [31]:

$$v = \frac{\mathrm{d}d}{\mathrm{d}t} = -\frac{(2\pi f p_a)^2}{27\eta}\rho\kappa^2\frac{R_0^5}{d^2}; \tag{11}$$

where d is the distance between the centres of the two bubbles and κ is the compressibility of the bubble. Integrating from the initial distance between the bubbles d_0 to 0 yields the collision time (Eqn. 12) shown in Fig. 9.

$$t_c = -\int_{d_0}^{0}\frac{27\eta}{(2\pi f p_a)^2\rho\kappa^2 R_0^5}d^2\mathrm{d}d = \frac{9\eta}{(2\pi f p_a)^2\rho\kappa^2}\frac{d_0^3}{R_0^5}, \tag{11}$$

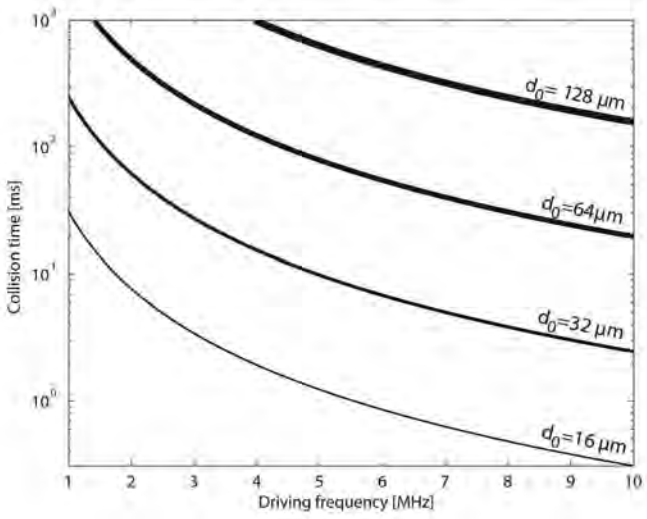

Figure 9 – Collision times of individual encapsulated microbubbles as a function of driving frequency at given distances $\boldsymbol{d_0}$, using $\boldsymbol{p_a} = \mathbf{20}$ kPa, $\boldsymbol{R_0}$ =1.25 μm, $\boldsymbol{\kappa}$ =5×10^{-6} m^2 N^{-1} and $\boldsymbol{\rho}$ =998 kg m^{-3}.

In a standing wave field, bubbles with resonance frequencies higher than the transmitted sound field aggregate at the pressure antinodes, whereas bubbles with resonance frequencies lower than the transmitted sound field aggregate at the pressure nodes [36]. Hence, the ultimate distance d_∞ between clusters must be a quarter of the wavelength, *i.e.*,

$$d_\infty = \frac{\lambda}{4} = \frac{c}{4f}. \tag{12}$$

Both processes of bubble clusters aggregating and the movement of clusters in the direction of the sound field can be described by a simplified version of Eqn. 6.

$$v = \frac{\mathrm{d}h}{\mathrm{d}t} \approx \frac{p_a^2}{6\rho c f \eta} \frac{\delta\left(\frac{f_c}{f}\right)}{\left[\left(\frac{f_c}{f}\right)^2 - 1\right]^2 + \left[\delta\left(\frac{f_c}{f}\right)\right]^2}, \tag{13}$$

where h is the distance travelled by the cluster and f_c is the cluster resonance frequency, for which $f_c < f_0$ must hold, since the bubble cluster radius $R_c > R_0$.

For the bubble cluster compressibility $\kappa_c, \kappa \leq \kappa_c < \kappa_f$ must hold, in which κ_f is the compressibility of a free (unencapsulated) gas bubble.

Bubble coalescence is the fusion of two or more bubbles. As adjacent bubbles collide or expand, the pressure in the film between them increases, resulting in a deformation (flattening) of the bubble surfaces. The continuing bubble expansion causes drainage of the interposed film. This thinning continues until a critical thickness around 0.1 μm is reached, at which the Van der Waals attractive forces result in film rupture and bubble coalescence [38]. Film drainage is generally much faster for free (unencapsulated) bubbles than for encapsulated bubbles, as a result of the flow pattern in the draining film [39].

The coalescence mechanism of lipid-encapsulated microbubbles was investigated, based on high-speed optical observations of sonicated ultrasound contrast agent microbubbles [39]. It was found that, when sonicated at high acoustic amplitudes, lipid-encapsulated microbubbles expose free surfaces during the expansion phase, speeding up the coalescence process dramatically. Hence, for the formation of bubble clouds or microfoams, the use of low acoustic amplitudes is desirable.

Materials and methods

A schematic overview of the experimental setup for simultaneous optical observation during sonication is shown in Fig. 10.

A polycarbonate container was built with internal dimensions of 24×18×15 $(cm)^3$. To give access to a microscope objective lens and reduce optic aberrations, a 11-mm diameter hole was drilled in the base, covered with a 2-mm thick test slide (Jencons (Scientific) Ltd., Leighton Buzzard, Bedforshire, UK). The container was filled with 2.6 L tap water. The container was locked in place on an $x - y$ translation stage of a DM IRM inverted microscope (Leica Microsystems GmbH, Wetzlar, Germany) with two objective lenses: a 506075 C-Plan 10×/0.22 NA objective lens (Leica Microsystems GmbH), and a 506236 N-Plan 50×/0.50 NA (Leica Microsystems GmbH) objective lens. A Mille Luce™ Fibre Optic Illuminator Model M1000 (StockerYale, Inc., Salem, NH) was connected to an optic fibre with a 7-mm diameter leading into the water of the container It was placed in line with the objective lens, as shown in Fig. 11.

The charge coupled device (CCD) of a FASTCAM MC-1 high-speed camera (Photron (Europe) Limited, West Wycombe, Bucks, United Kingdom) was mounted to the C-Mount of the microscope and connected to its processing unit, which was capable of recording images up to 10,000 frames per second. The camera was controlled by a laptop computer.

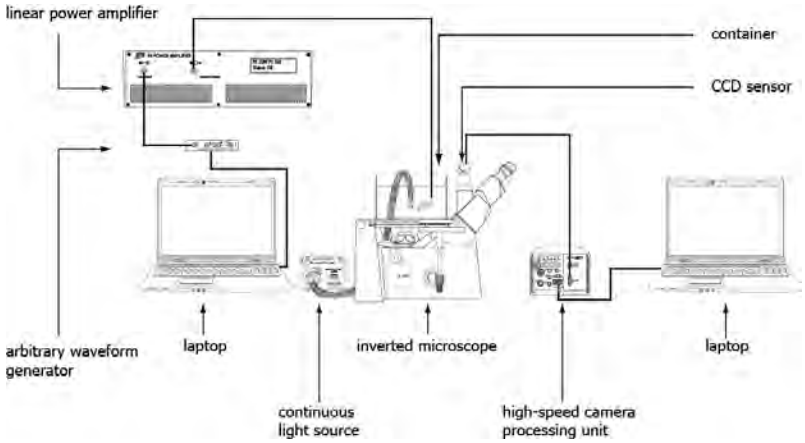

Figure 10 – Schematic overview of the experimental setup.

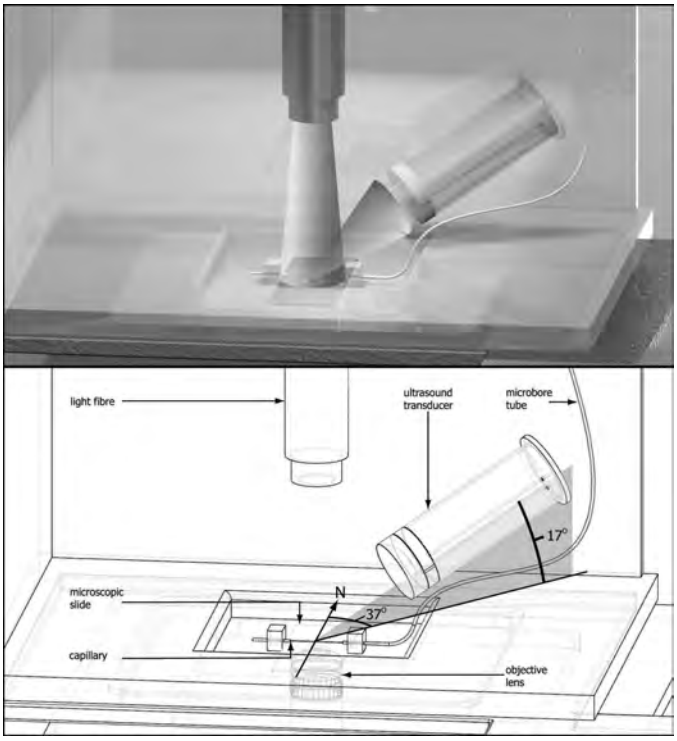

Figure 11 – Close-up of the sonication tank coinciding sound, light beam and objective focus (top) and definitions of the azimuth and elevation of the transducer relative to the North of the container (bottom).

Ultrasound

A laptop computer triggered a DATAMAN-530 arbitrary waveform generator (Dataman Programmers Ltd., Maiden Newton, Dorset, UK), which was connected to a 2100L, 50-dB RF power amplifier (Electronics & Innovation Ltd., Rochester, NY). The power amplifier was connected to a single element transducer containing a Pz37 Piezoelectric ceramic (Ferroperm Piezoceramic A/S, Kvistgård, Denmark) with a centre frequency of 2.2MHz. The design of the transducer is shown in Fig. 2. Transmitted signals were continuous waves with frequencies in the range 1–10MHz. The peak-negative acoustic pressures were determined using a PVDF needle hydrophone system with a 0.2-mm active element (Precision Acoustics Ltd., Dorchester, Dorset, UK) connected to a TDS 420A digitising oscilloscope (Tektronix, Inc., Beaverton, OR).

The ultrasound transducer was positioned in the container using a clamp stand, at a focal distance of 38mm from the region of interest to be studied. The azimuth of the length axis of the transducer to the relative North of the container was 37º and the elevation of the length axis of the transducer relative to the base of the container was 17º, as shown in Fig. 11.

Ultrasound contrast agent

Definity® (Lantheus Medical Imaging, North Billerica, MA) consists of C_3F_8 gas microbubbles with mean diameter between 1.1 and 3.3 μm, encapsulated by a lipid/surfactant shell. Its resonance frequency has been measured to be 2.7MHz [61]. The 1.5-ml vials used in these experiments were stored at 9ºC. Each vial was shaken for 15 s using a Vialmix® device (Lantheus Medical Imaging, North Billerica, MA). Before introducing the ultrasound contrast agent, it was further diluted using a 0.9% saline solution.

The diluted ultrasound contrast agent was inserted using a syringe into a micro-bore tube with a 0.51-mm inner diameter. The tube led to a CUPROPHAN® RC55 cellulose capillary (Membrana GmbH, Wuppertal, Germany) with a 200-μm inner diameter and 8-μm wall thickness. The middle of the capillary coincided with the optical focus of the objective lens and with the acoustic focus of the ultrasound transducer, as shown in Fig 11. The typical field of view using the 10× objective lens was 500×500 $(\mu m)^2$, whereas the diameter of the acoustic focus was greater than 5mm. Hence, the whole field of view could be considered in acoustic focus.

The capillary was positioned 2 mm above base of the container. The flow speed of the ultrasound contrast agent through the capillary was manually controlled.

In total, 48 experiments were performed. Bubble and cluster sizes were measured and tracked using Image-Pro Plus (Media Cybernetics, Inc., Bethesda, MD). Further analysis was done using Matlab® (The Mathworks™, Natick, MA).

Results and discussion

At the high concentration used, clustering started instantaneously after the ultrasound source activated. Fig. 12 illustrates the speed of cluster formation of DEFINITY® ultrasound contrast agent that had been further diluted to 1:20 v/v.

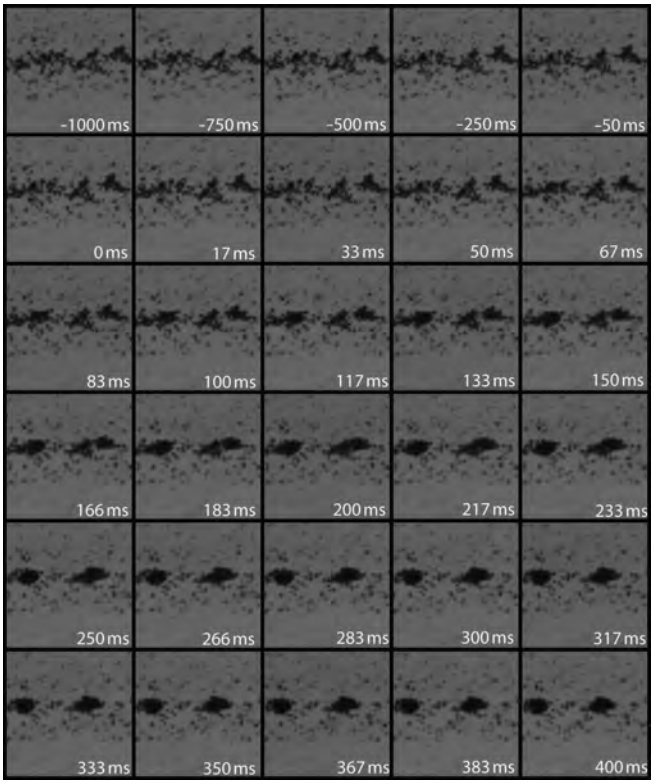

Figure 12 – Microfoam formation during continuous sonication at 2 MHz and 20-kPa peak-negative acoustic pressure. Each frame corresponds to a 120×120 (μm)² area. Time $\boldsymbol{t = 0}$ was defined by the start of the sonication.

With distances between microbubbles of only few micrometres, collision times from Eqn 11 should be within a second, as shown in Fig. 9. Also from Eqn. 11 and Fig. 9 it is explained why cluster formation must be faster at higher frequencies, if the other acoustic parameters and the concentration are not changed, or, after a fixed duration, larger clusters must have formed using higher frequencies, since bubbles can approach from larger d_0 at higher f. These deductions are confirmed by the following experimental observations. In Fig. 12, after 233 ms two clusters have been formed of approximately 15 μm diameter each. These started to approach in the subsequent frames. Overall, newly formed clusters collided to form larger clusters. This is illustrated in figures 13 and 14.

Each branch represents a cluster. The branches coming together represent the collision and coalescence of clusters into larger clusters. The velocities of clusters are on the order of tens of micrometres per second. Although increasing the acoustic pressure would increase the cluster velocities dramatically, as evident from Eqn. 13, they would also lead to microbubble disruption [22]. At the frame rates used phenomena associated with microbubble disruption were not observed.

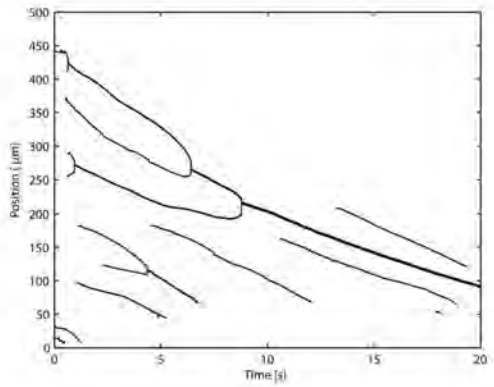

Figure 13 - Cluster positions as a function of time, during continuous sonication at 2 MHz and 20-kPa peak-negative acoustic pressure. Position in the capillary is defined from East (0 µm) to West (500 µm). Bold lines indicate merged clusters. The beginning (left) of a line indicates the formation of a cluster of diameter > 6.8 µm. The end (right) of a line indicated the disintegration or contraction of a cluster to a diameter < 6.8 µm.

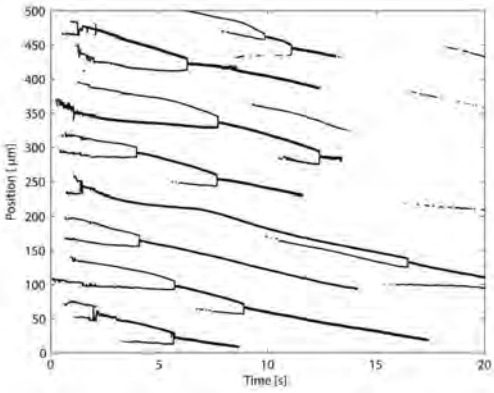

Figure 14 - Cluster positions as a function of time, during continuous sonication at 7 MHz and 22-kPa peak-negative acoustic pressure. Position in the capillary is defined from East (0 µm) to West (500 µm). Bold lines indicate merged clusters. The beginning (left) of a line indicates the formation of a cluster of diameter > 6.8 µm. The end (right) of a line indicated the disintegration or contraction of a cluster to a diameter < 6.8 µm.

The larger a cluster grows, the lower its resonance frequency becomes. Hence, the velocity of a cluster in the direction of the sound field, defined by Eqn. 13, should decrease in time. If two identical clusters with resonance frequency f_0 merge, the resulting resonance frequency is $f_c' \approx \left(2^{-\frac{1}{3}}\right) f_0 = 0.79 f_0$ [110]. Assuming that the compressibility and damping coefficient do not substantially change, a similar decrease in cluster velocity is expected. However, the decrease in slope magnitude of the main branch in Fig. 13 is negligible. This might be explained if the resulting cluster is much stiffer than the original clusters, increasing the damping coefficient.

Also, 7 MHz must be further off the cluster resonance frequency than 2 MHz. Hence; the magnitudes of the slopes in Fig. 14 are lower than those in Fig. 13.

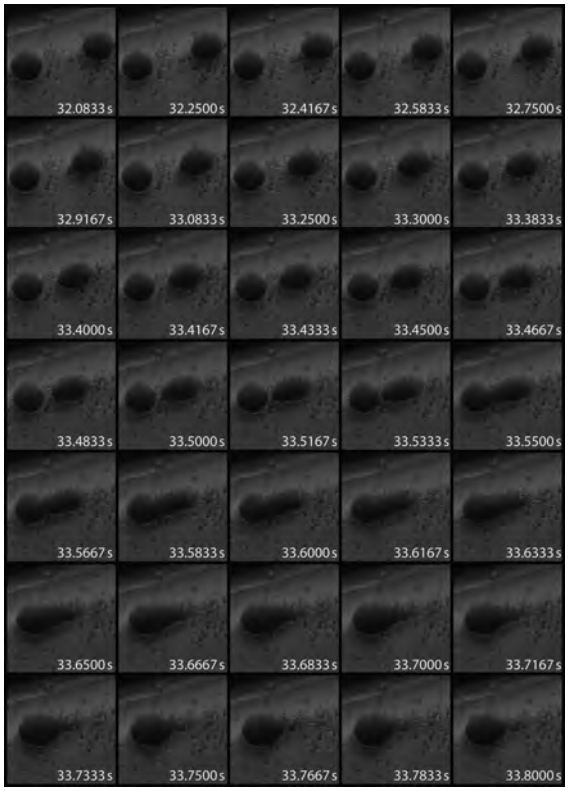

Figure 15 – Two clusters, with 22-μm diameters and an initial distance of 55-μm, colliding and merging during continuous sonication at a 2–MHz driving frequency and a 20-kPa peak-negative pressure. The frame size corresponds to 81×81 (μm)². Times are relative to the start of the sonication ($\boldsymbol{t = 0}$).

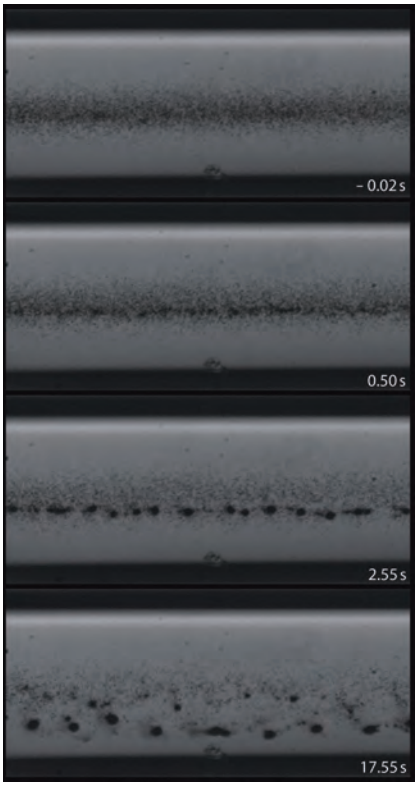

Figure 16 – Clusters forming during sonication at 7 MHz and 22-kPa peak negative pressure. The frame size corresponds to 560×264 (μm)². Time $t = 0$ was defined by the start of the sonication.

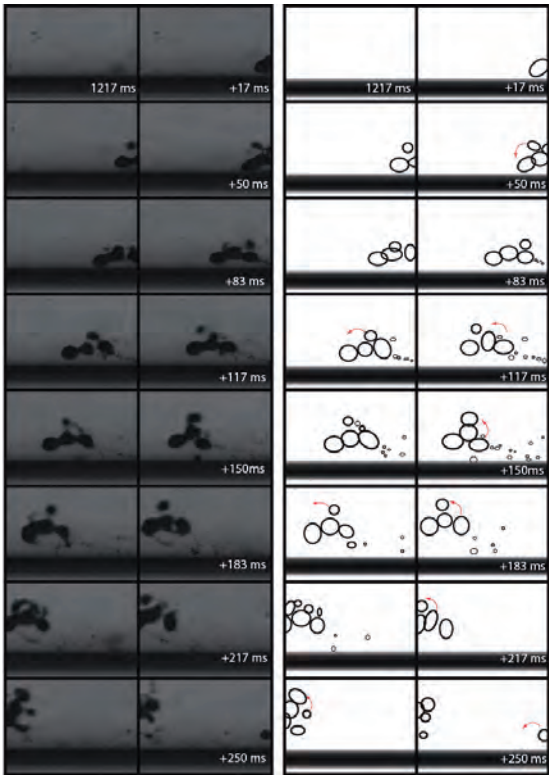

Figure 17 – Morphing microfoam during sonication at 7 MHz and 86 kPa peak-negative pressure and a schematic representation of the event. The frame size corresponds to 274×198 (μm)2. Time $t = 0$ was defined by the start of the sonication.

Secondary radiation forces of clusters onto each other do not explain the cluster colliding times observed. Even if the compressibility of the clusters would be equal to that of a single ultrasound contrast agent microbubble, under the acoustic conditions used the collision times from Eqn. 11 would be just milliseconds.

Hence, the bubble clusters cannot be regarded as identical monopoles in this setting.

A close-up of two colliding clusters with 22-μm diameters forming a 25-μm cluster is shown in Fig. 15. The total time spanning this process is slightly less than 1.8 s.

The clusters were initially formed in the middle of the capillary. These clusters were located at distances $d_0 < \frac{1}{4}\lambda$, as demonstrated in Fig. 16. However, following further cluster coalescence during 17.55 s of sonication, the final distance between the larger

clusters corresponded to $\frac{1}{4}\lambda = 54$ μm. These had been pushed towards the lower capillary wall, owing to primary radiation forces.

The clusters velocities towards the capillary wall were between 5 μm s^{-1} at 7 MHz and 22-kPa peak-negative pressure and 15 μm s^{-1} at 2 MHz and 20 kPa peak-negative pressure sonication. These are of the same order as the left hand side term in Eqn.13. The magnitudes of the slopes in Fig. 14 did not change close to the capillary wall. Hence, in this experimental setup, any effect of the capillary wall on cluster translation was neglected.

At these bulk concentrations, clusters were formed within seconds with diameters 25±2 μm. Taking into account the diameters and assuming a spherical shape, it can be estimated that the clusters contain 2,000 microbubbles each.

The clusters interact, owing to primary and secondary Bjerknes forces, creating morphing microfoams. Figure 17 shows four interacting clusters in steady liquid.

Primary Bjerknes forces push the clusters in the direction of the sound field at an average speed of 4 mm s^{-1}. The shear of the capillary wall caused a rotation of the interacting clusters.

Figure 18 shows at least eight interacting clusters. Again, a rotation motion can be observed. Also, individual ultrasound contrast agent microbubbles can be seen to hop from cluster to cluster. This microscopic scale behaviour can be attributed to very subtle changes in the acoustic field, causing ever-changing local nodes and antinodes. With cluster diameters less than 30 μm, buoyancy effects may be neglected at these timescales as well.

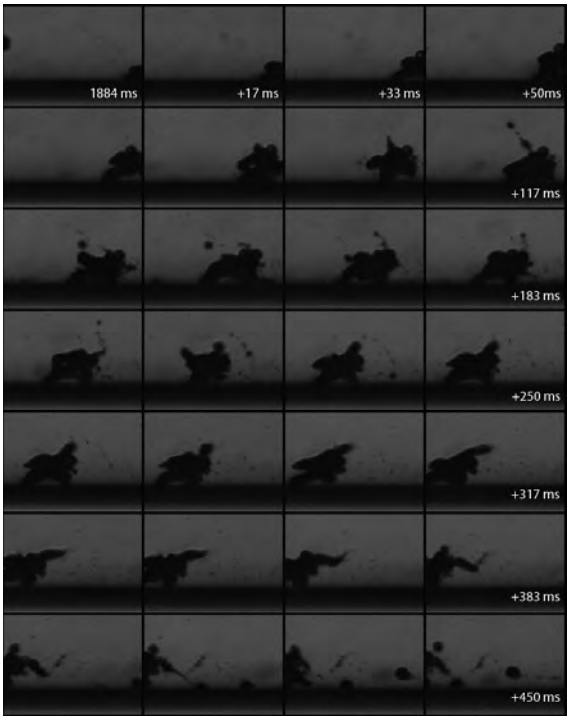

Figure 18 - Morphing microfoam during sonication at 7 MHz and 86 kPa peak-negative pressure and a schematic representation of the event. The frame size corresponds to 274×198 (μm)². Time $\boldsymbol{t = 0}$ was defined by the start of the sonication.

In summary, the following stages of microfoam formation, illustrated in Fig. 19 were observed. The initial situation was a dense, random bubble distribution before ultrasound arrival. After sonication started, contrast microbubbles collided, owing to secondary radiation forces. Subsequently, these clusters merged within the space of a quarter of the wavelength, owing to primary radiation forces. The resulting microfoams translated in the direction of the ultrasound field, owing to primary radiation forces.

Small deviations in microbubble sizes or shell properties lead to deviations in individual bubbles' resonance frequencies, as expressed in Eqn. 8. These in turn cause oscillation phase differences, as expressed in Eqn. 6, big enough to be observed [40]. Therefore, predicting and manipulating individual microbubbles is technically challenging. It has been demonstrated that as soon as the bubble clusters were formed and as long as they were in the sound field, they behaved as one entity. At the acoustic settings used, it took seconds to force the bubble clusters to positions approximately $\frac{1}{4}\lambda$ apart. It also just took seconds to drive the clusters towards a boundary.

It may assume that vessel blocking can only be successful if a microfoam is created with a diameter equal to or greater than the vessel diameter d_v. From this study it follows that in order to create such a foam, $\frac{1}{4}\lambda > d_v$, or, $f < \frac{c}{4d_v}$.

For therapeutic purposes, it would be of great interest to induce microjetting on entire clusters towards a vessel wall, presumably causing sonoporation or sonolysis.

Although ultrasound-induced microjetting has been observed with ultrasound contrast agents, its occurrence in *in vivo* situations is hard to control [41, 42].

Predictable sonic manipulation would be better feasible if the microbubbles would be forced to cluster to known size and position first.

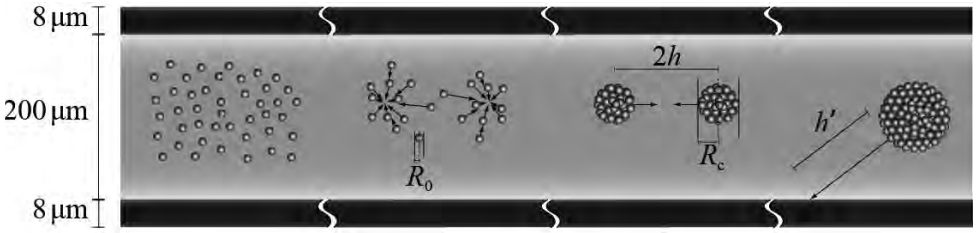

Figure 19 – Schematic representation of the four stages of microfoam formation in a capillary: (left-right) random bubble distribution before ultrasound arrival, bubble colliding during sonication, cluster mergence within the space of a quarter of the wavelength, microfoam translation.

Conclusions

The following stages of microfoam formation within a densely populated concentration of microbubbles were observed. After the sonication started, contrast microbubbles collided, forming small clusters, owing to secondary radiation forces.

These clusters coalesced within the space of a quarter of the ultrasonic wavelength, owing to primary radiation forces. The resulting microfoams translated in the direction of the ultrasound field, hitting the capillary wall, also owing to primary radiation forces.

It has been demonstrated that as soon as the bubble clusters were formed and as long as they were in the sound field, they behaved as one entity. At the acoustic settings used, it took seconds to force the bubble clusters to positions approximately a quarter wavelength apart. It also just took seconds to drive the clusters towards the capillary wall.

Subjecting ultrasound contrast agent microbubbles to a continuous low-amplitude signal makes them cluster to known positions and known microfoam sizes, allowing for straightforward sonic manipulation.

Sonoporation at a low MI

Introduction

Sonoporation is the transient permeabilisation and resealing of a cell membrane with the help of ultrasound and/or an ultrasound contrast agent, allowing for the trans-membrane delivery and cellular uptake of macromolecules between 10 kDa and 3 MDa [29]. Many studies have demonstrated increased drug and gene uptake of sites under sonication [28, 43-49]. These studies presumed, that a physical membrane disruption mechanism, *i.e.*, sonoporation, caused the increased uptake, as opposed to naturally occurring active uptake processes, such as endocytosis, that are controlled by the system biology [28, 43-49].

Although mechanical disruption with the aid of ultrasound has been attributed to violent side effects of inertial cavitation and microbubble fragmentation, most notably, the increased uptake has also been observed at low acoustic amplitudes, *i.e.*, in acoustic regimes where inertial cavitation and microbubble fragmentation are not to be expected [50]. An ultrasound contrast agent microbubble might act as a vehicle to carry a drug or gene load to a perfused region of interest. If the same ultrasound field that has been implicated in the sonoporation process can cause release of the therapeutic load, this load could be delivered into cells. Apart from plainly mixing ultrasound contrast agents with therapeutic agents, several schemes have been proposed to incorporate therapeutic loads to microbubbles. These include loads to the microbubble shell [51], therapeutic gases inside the microbubble [52], gas-filled lipospheres containing drugs [53], and drug-filled antibubbles [54]. To understand and ameliorate ultrasound-assisted drug and gene delivery, the physics of controlled release and of sonoporation have been under investigation. That objective also forms the focus for this chapter. Moreover the behaviour of ultrasound contrast agent microbubbles near cancer cells deliberately at low acoustic amplitudes in order to probe whether sonoporation in this regime was possible was studied; and if so, to ascertain what the microscopic mechanism might entail; and finally, to assess and scrutinise the safety aspects of ultrasound exposure in this regime.

Mechanical index

On commercial scanners, the MI has been limited to 1.9 for medical imaging [55]. At low MI, microbubbles pulsate linearly, whereas at high MI, their greater expansion phase is followed by a violent collapse. During the collapse phase, when the kinetic energy of the bubble surpasses its surface energy, a bubble may fragment into a number of smaller bubbles. Fragmentation has been exclusively observed with contrast agents with thin, elastic shells. Fragmentation is the dominant disruption mechanism for these bubbles [22]. Although the fragmentation of therapeutic load-bearing microbubbles must release their loads, the actual drug or gene delivery is in this case a passive process, dependent on diffusion rate and proximity to the target cells. Fragmenting microbubbles may not create pores in cells, since fragmentation costs energy. However, if a microbubble collapses near a free or a solid boundary, the retardation of the liquid near the boundary may cause an asymmetry. This asymmetry

causes differences in acceleration on the bubble surface. During further collapse, a funnel-shaped jet may protrude through the microbubble, shooting liquid to the boundary [56]. The pore size created by a jet has been empirically related to the microbubble expansion [57]. If jets could be directed to cell layers, in case of a microbubble carrying a therapeutic load, the load could be delivered into cells. The jet formation is affected by the cavitation topology, synergistically interacting with local fluid dynamics arising through the bubble's expansion and contraction due to the ultrasound field. However, as the fluid forming the microjet is just the bulk fluid that carries no therapeutic agent, then there is no guarantee that, even with the formation of a sonopore due to jet impact with the cell membrane, therapeutic agent will enter the cell. It needs to be dislodged and mobilised from the bubble first. Furthermore, jetting has not been observed at low or moderate MI [41], so that fragmentation is likely to occur before any delivery takes place. By pushing the loaded microbubbles towards the vessel all using primary radiation forces [30], release can take place closer to target vessels. In a recent study, Caskey *et al*. pushed bubbles into tissue-mimicking gels at MI=1.5 [58]. It was previously studied how microclusters consisting of lipid-encapsulated microbubbles can be formed using primary and secondary radiation forces, and how these clusters can be pushed towards vessel walls [59]. It was found that, even at MI<0.15, microbubble clusters can be formed and pushed towards a boundary within seconds.

Sonoporation

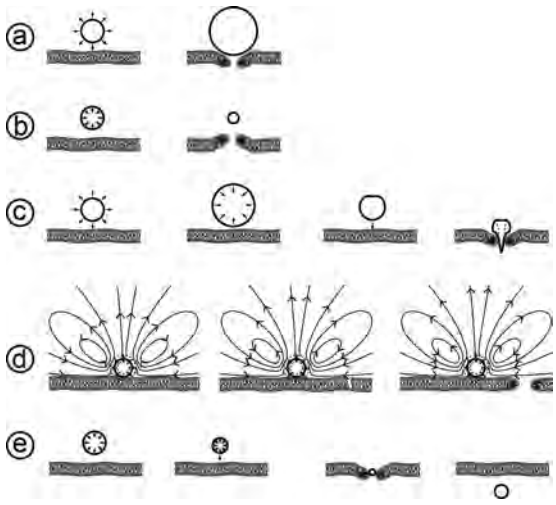

Figure 20 – Possible mechanisms of sonoporation: (a) push, (b) pull, (c) jetting, (d) shear, (e) translation.

There are five non-exclusive hypotheses for explaining the sonoporation phenomenon. These have been summarised in Figure 20: push, pull, jetting, shear, and translation [60]. It has been hypothesised that expanding microbubbles might push the cell membrane inward, and that collapsing bubbles might pull cell membranes outward [61]. These mechanisms require microbubbles to be present in the close vicinity of cells. A separate release mechanism should then ensure localised delivery. Although jetting only occurs in a high-MI regime, it is very effective in puncturing cell membranes. Jetting has been observed through cells using ultrasound contrast agent microbubbles. However, the acoustic impedance of the solid cell substratum formed the boundary to which the jetting took place, not the cell itself [42]. Also, there has not been any proof yet of cell survival after jetting. In a separate study, the role of jetting as a dominant mechanism in sonoporation was excluded [62]. If a microbubble is fixed to a membrane the fluid streaming around the oscillating bubbles creates enough shear to rupture the membrane [63]. Here again, separate release mechanisms should then ensure localised delivery. Finally, it has been speculated that lipid-encapsulated microbubbles, in compressed phase, translate through cell membranes or channels in the cell membrane such as the receptor. In case of therapeutic loading, the load would be delivered directly into the target cell. The main advantage of the latter mechanism is that microbubble translation by means of ultrasonic radiation forces requires very low acoustic pressures. Hence, potential damaging bioeffects due to inertial cavitation can be ruled out.

Materials and methods

Sonoporation configuration

In previous studies, increased gene uptake was demonstrated at MI<0.3 [64, 65]. Similar sonoporation configuration was used for these experiments. An overview of the experimental setup is shown in Figure 21. A signal consisting of 50 cycles with a centre frequency of 6.6MHz and a pulse repetition frequency of 10 kHz, i.e., a duty cycle of 7.5%, was generated by an AFG3102, dual channel arbitrary function generator (Tektronix, Inc., Beaverton, OR), amplified by a 150A250 radio-frequency (RF) amplifier (Amplifier Research, Souderton, PA) set to maximum gain, and fed to a custom-built 6.6-MHz ultrasound transducer with a hexagonal Y-36º lithium niobate element with a maximum diameter of 25mm [66].

The peak-negative acoustic pressure was measured to be 0.5 MPa in a separate tank and in the sonication chamber itself. This corresponds to an MI of 0.2.

The transducer was placed in a custom-built, 260×160×150 $(mm)^3$ Perspex sonication chamber, in which an OptiCell® cell culture chamber (Nunc GmbH & Co. KG, Langenselbold, Germany) was placed. One side of the cell culture chamber contained a monolayer of 1.6×10^6 HeLa cells that had been cultured in MEM with Earl's salts medium (PAA Laboratories GmbH, Pasching, Austria) supplemented with 10% v/v heat-inactivated foetal calf serum, GlutaMAX™ (Life Technologies Gibco, Paisley, Renfreshire, UK), 1% v/v of non-essential amino-acids (PAA), penicillin (100 units ml^{-1}) and streptomycin (100 µg ml^{-1}) (PAA), at 37ºC in a humidified atmosphere containing

5% CO_2. The cells were used when there was 60–80% confluency. Ultrasound contrast agent was injected into the cell culturing chamber before each experiment. Several lipid-shelled ultrasound contrast agents were tested in this study. In this chapter, results of a 3.33% dilution of MicroMarker® (VisualSonics B.V., Amsterdam, Netherlands), a lipid-shelled agent with a mean diameter of 2.5 μm are presented. A customised BXFM-F microscope unit with an LCAch N 20×/0.40 NA PhC (Olympus Deutschland GmbH, Hamburg, Germany) and a LUMPlanFL 60×/0.90 NA water-immersion objective (Olympus) was placed on top of the sonication chamber with the objective lens immersed in the water. The colour charge coupled device (CCD) of a PHOTRON FastCam MC-2.1 high-speed camera (VKT Video Kommunikation GmbH, Pfullingen, Germany) was connected to the microscope. The sensor was rotated to make sure that in all recorded movies, the ultrasound is directed from the left to the right of the frame.

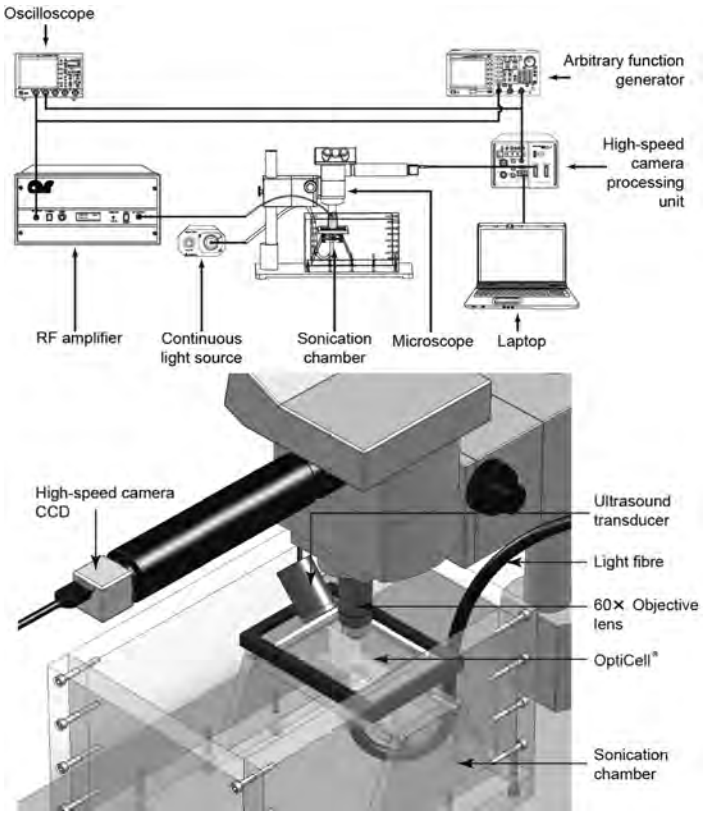

Figure 21 – Experimental setup (*top*) and a close-up of the sonoporation configuration (*bottom*).

Fluorescence configuration

An overview of the setup used for the fluorescence experiments is shown in Fig 22. It is almost identical to the setup described in the previous section. However, here, the signal consisted of 40 cycles with a centre frequency of 6.6MHz and a pulse repetition frequency of 10 kHz, *i.e.*, a duty cycle of 6.1%, was amplified using a 2100L, 50-dB RF amplifier (Electronics & Innovation Ltd., Rochester, NY) and fed to a custom-built 6.6-MHz ultrasound transducer [66]. In this configuration the ultrasound propagated from the bottom-right, to the top-left of the frame.

Prior to injection in the OptiCell®, the MicroMarker® contrast agent was labeled using a DiD ($DiIC_{18}(5)$) lipophilic fluorescent probe (Vybrant™ Molecular probes, Invitrogen, San Diego, CA). A ratio of 1 µl of DiD to 40 µl MicroMarker® was homogenised by pipetting and incubating for 5 minutes at room temperature.

Figure 23 shows how the DiD fluorescent probe bonded to the phospholipid [67]. Emitted fluorescence ($\lambda = 649$–703 nm) was localised on the microbubble shell when exciting at $\lambda = 633$ nm.

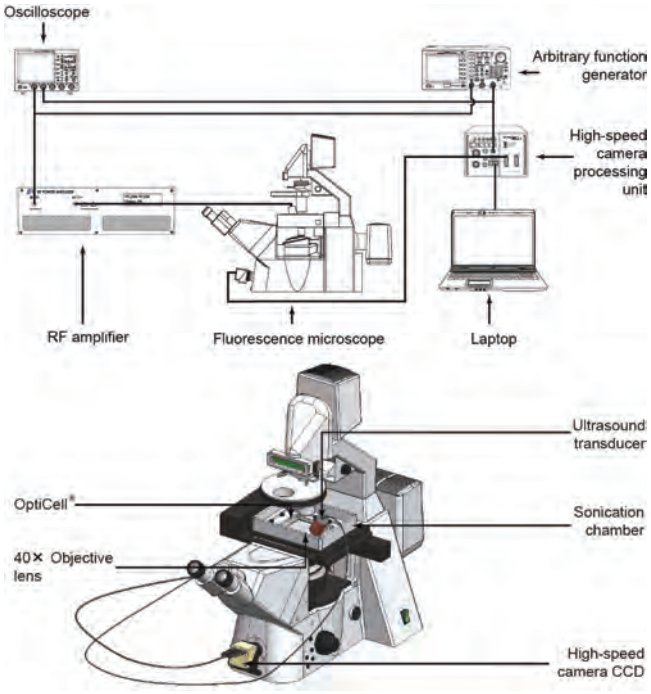

Figure 22 – Experimental setup (top) and a close-up of the fluorescence configuration (bottom).

A custom-made aluminium sonication chamber with internal dimensions of 130×170×35 $(mm)^3$ was locked into to the $x-y$-stage of a 200M inverted confocal microscope (Carl Zeiss AG, Oberkochen, Germany) coupled with a LSM Axiovert 510 laser scanning

device (Carl Zeiss), using an EC Plan-Neofluar 40×/1.30 NA Oil DIC M27 objective (Carl Zeiss AG), with automated $z-$stack functionality. The peak-negative acoustic pressure was measured at the objective's field of view and corresponded to MI=0.2.

To evaluate the possible electrostatic attraction between microbubbles and cells, 30 µl MicroMarker® was diluted into 700 µl of distilled water and tested for electrophoretic mobility (ζ -potential) using a Zetasizer 3000 (Malvern Instruments, Malvern, Worcestershire, United Kingdom).

To measure the thickness of the cultured cells 10^5 HeLa cells were seeded into an OptiCell®. The cell plasma membrane was labelled with DiD lipophilic fluorescent probe (Vybrant™ Molecular probes) according to the manufacturer's protocol. The membrane fluorescence was measured using a 200M confocal microscope (Carl Zeiss). Cell thickness was calculated from the difference between the upper and lower slices where fluorescence was seen. In all fluorescence recordings, the slice thickness was set to <1 µm.

Twenty-three movies under 6.6-MHz sonication at frame rates between 500 and 2000 frames per second, representing 15 minutes of real-time exposure were recorded. Of these, 11 movies were recorded using fluorescence. In addition 10 control movies were recorded, with a total duration of 22 minutes.

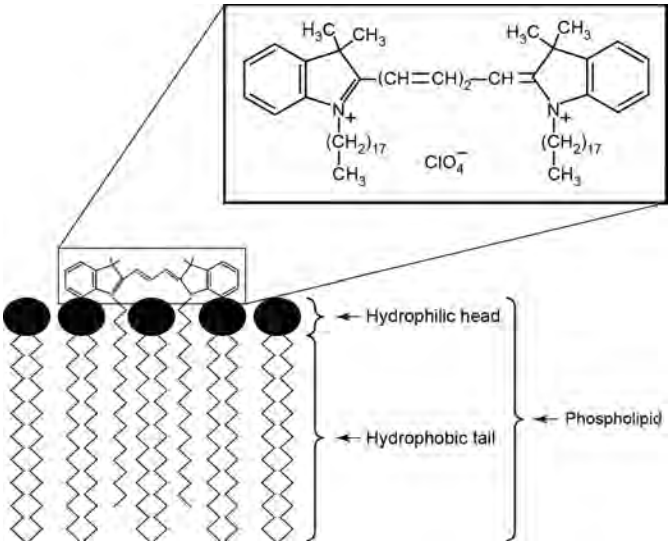

Figure 23 - Schematic representation of DiD [DiIC$_{18}$(5)] lipophilic fluorescent probe bonding to phospholipid.

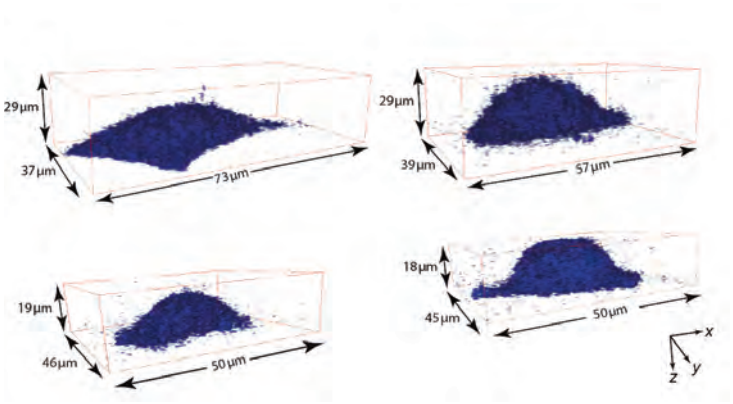

Figure 24 - z –stacks of fluorescence emitted by the DiD dye attached to the membranes of four typical HeLa cells, representing the cell geometry.

Results and discussion

Throughout this section, the optical z –axis is defined from distal-to-focus (negative) to proximal-to-focus (positive), with $z = 0$ as the focal plane.

Figure 24 shows z –stacks of fluorescence emitted by the DiD dye attached to the membranes of four typical HeLa cells, representing the cell geometry. In total, the thicknesses of 42 cells were measured. The cultured cells were found to be 13±2 µm thick. Clearly, these cells had thicknesses much greater than ultrasound contrast agent microbubble oscillations amplitudes at MI=0.2.

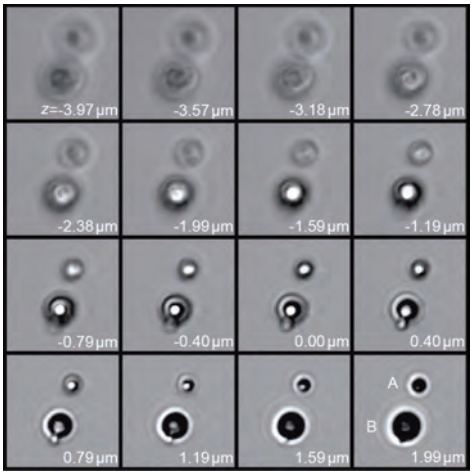

Figure 25 – z –stack of two ultrasound contrast agents microbubbles. Proximal-to-focus Airy disks can be seen around the bubbles, whereas distal-to-focus the bubble boundaries are blurred.

Microbubble "A" has a diameter of 2 µm, whereas microbubble "B" has a diameter of 3 µm. Each frame corresponds to a 11×11 (µm)2 area.

The optical system was analysed and the results were compared to bubbles and cells that were slightly out of focus, to rule out that the movement of the bubble takes place in a plane different from that of the cell. Figure 25 shows a z –stack of two ultrasound contrast agent microbubbles, similar to Figure 10 of Postema *et al* [68]. Proximal-to-focus Airy disks can be seen around the bubbles, whereas distal-to-focus the bubble boundaries are blurred. Note that the boundary contrast is maximal just proximal-to-focus [68].

At a centre frequency of 6.6 MHz, 17 events of microbubbles entering HeLa cells were recorded. After entering, the microbubbles were observed to quickly dissolve. As an example, Figure 26 shows an event resampled at 3.4 Hz and 40 Hz, respectively, here two bubbles were pushed to a cell during 11 s of sonication.

A microbubble "A" of 4-µm diameter entered the cell and dissolved, whereas a microbubble "B" of 2-µm diameter stuck to the cell membrane.

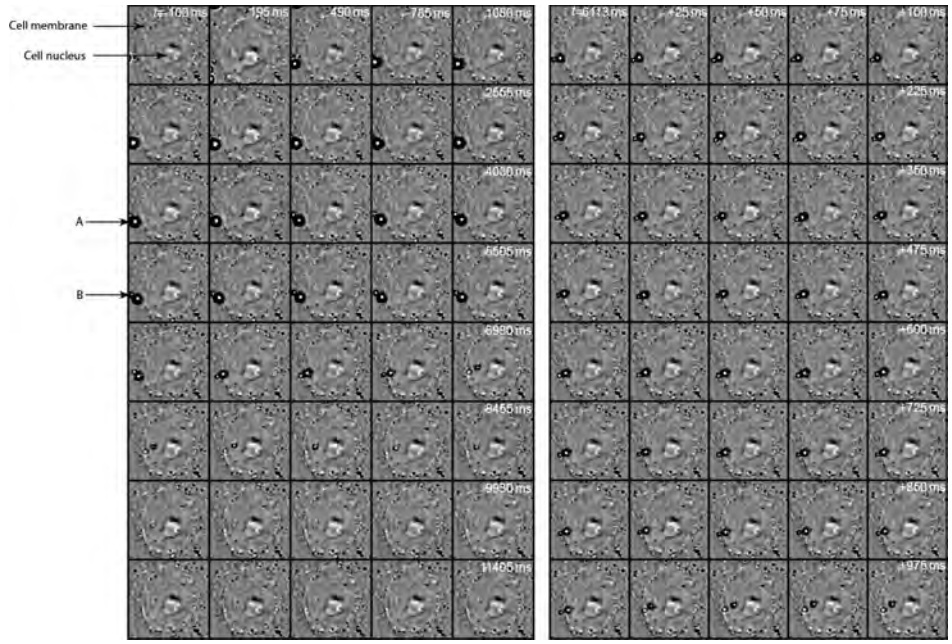

Figure 26 - A sonoporation event including microbubble dissolution during 11 s of sonication (*left*) and selected frames of the microbubble entering a cell (*right*). Microbubble "A" entered the cell and dissolved, whereas microbubble "B" stuck to the cell membrane. Each frame corresponds to a 23×23 $(\mu m)^2$ area.

Figures 27 and 28 show two similar events, where fluorescence-coated microbubbles were used. The left panels show a microbubble apparently penetrating through the cell membrane in optical focus. Approximately 70ms after the ultrasound is switched on a microbubble is seen to penetrate through the cell membrane in Figure 27. In Figure 28 the microbubble is seen to penetrate through the cell membrane approximately 24 ms after the ultrasound has been switched on. The right panels show a z –stack through the entire cell, to record whether the apparent microbubble entry is actually into the cell. For both events, Figure 29 shows average fluorescent intensities in two regions of interest, one inside the cell, and one control region. In both events, most fluorescence from apparent microbubble entry can be observed within 5 μm proximal to optical focus, thus well within the cells themselves.

Figure 30 shows frames in optical focus from the events in Figures 27 and 28, before sonication and approximately 8 minutes after sonication. Clearly, fluorescence has transferred into the cells and remained inside the cells long after sonication. At these low acoustic amplitudes, inertial cavitation, fragmentation, and jetting should not occur. Hence, as a mechanism in sonoporation at low MI, these phenomena might justifiably be neglected.

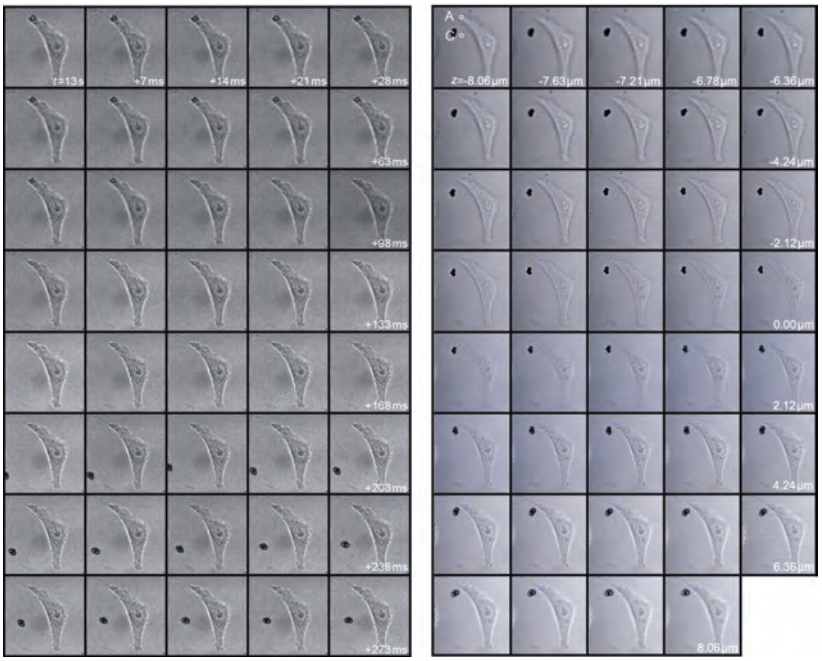

Figure 27 - Microbubble of 5-μm diameter apparently penetrating through he cell membrane in optical focus (*left*); $\boldsymbol{z}$ –stack through the entire cell, to record whether the apparent microbubble entry is actually into the cell (right). Areas "A" and "C" are regions of interest inside and outside the cell, respectively. Each frame corresponds to a 76×76 $(\mu m)^2$ area.

Our observations do not explain why some microbubbles enter a cell and others don't. The quick dissolution after entering suggests that the microbubble loses (part of) its shell whilst entering.

The ζ potential measurements showed that the microbubble shells had a charge of −43.9±2.4mV. As cells have a natural negative charge [69, 70], the ultrasound contrast agent should be repelled by the cells. In all recordings it was seen that once the ultrasound was turned on, the microbubbles were attracted to the closest cell, independent of the direction of the sound field. This supports the recent finding that cell membranes can be acoustically active [71], and therefore interact with microbubbles.

Other cell types than HeLa cells must be used in follow-up studies, to investigate differences in bubble−cell interaction.

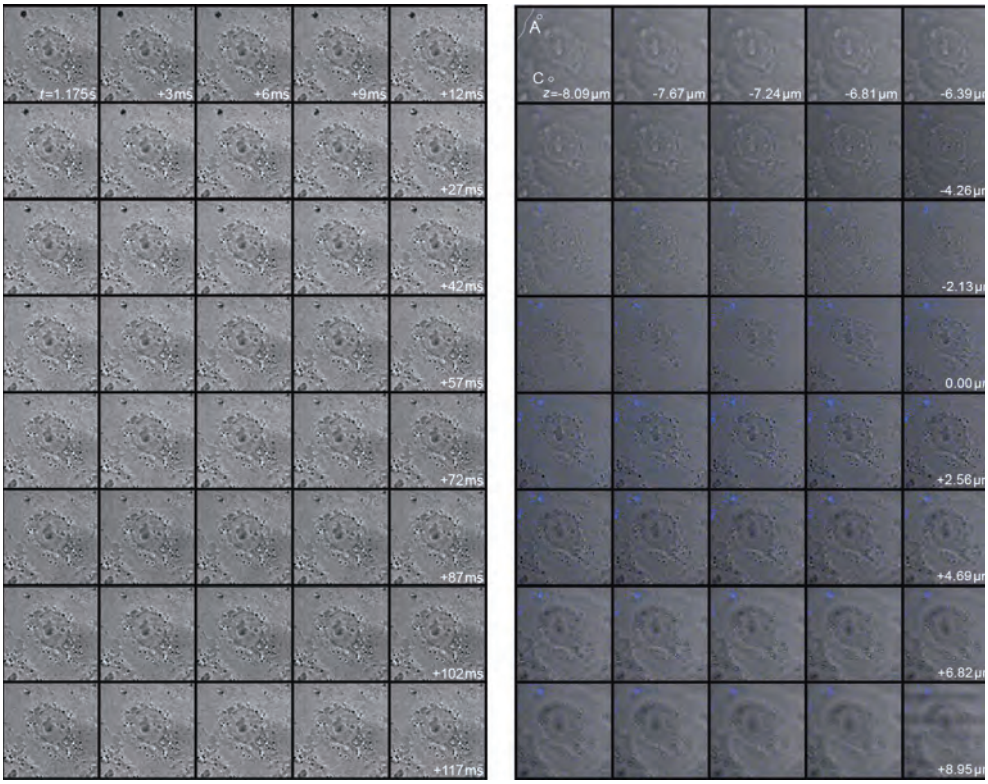

Figure 28 – Microbubble of 4-µm diameter apparently penetrating through he cell membrane in optical focus (*left*); z −stack through the entire cell, to record whether the apparent microbubble entry is actually into the cell (right). Areas "A" and "C" are regions of interest of high fluorescence and low fluorescence, respectively. The white dotted line in the upper left frame of the right panel indicated the cell membrane. Each frame corresponds to a 52×52 $(\mu m)^2$ area.

Conclusions

It has been demonstrated that lipid-shelled microbubbles can be forced to enter cells at a low MI. Hence, if a therapeutic load is added to the bubble, ultrasound-guided delivery could be facilitated at diagnostic settings. In addition, these results may have implications for the safety regulations on the use of ultrasound contrast agents for diagnostic imaging.

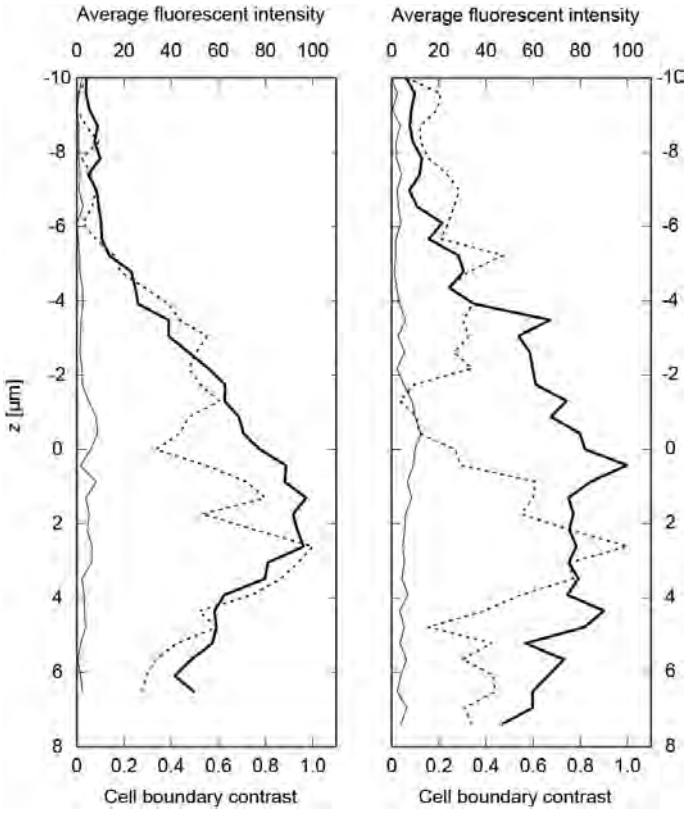

Figure 29 - Average fluorescent intensities in the regions of interest (ROI) of Figures 27 (*left*) and 28 (*right*). Bold lines represent the ROI "A" inside the cells, whereas hairlines represent ROI "C" the control regions. The dotted line represents the cell boundary contrast. Note that the cell boundary is maximal just proximal-to-focus.

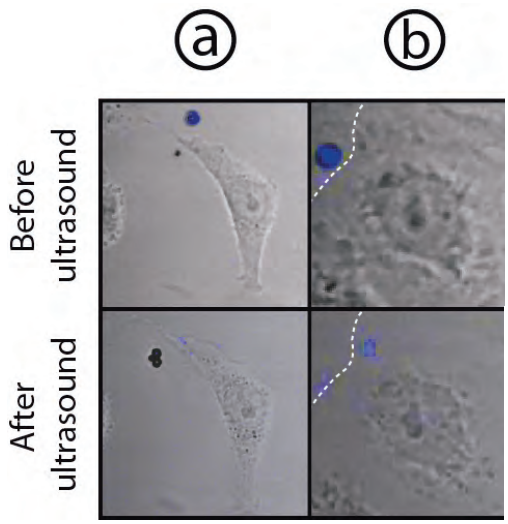

Figure 30 – Columns (a) and (b) represent frames in optical focus from the events in Figures27 and 28, respectively, before sonication and approximately 8 minutes after sonication. The white dotted line in the right frame indicates the cell boundary. The left frames correspond to 76×76 $(\mu m)^2$ areas, whereas the right frames correspond to 45×45 $(\mu m)^2$ areas.

References

1. Unger, E.C. et al., *Therapeutic applications of microbubbles.* Eur. J. Radiol., 2002. 42: p. 160-168.
2. Stewart, I., P.J. Schluter, and G.R. Shaw, *Cyanobacterial lipopolysaccharides and human health: a review.* Environ. Health, 2006. 5(7): p. 1-23.
3. Fleming, L.E. et al., *Blue green algal (cyanobacterial) toxins, surface drinking water, and liver cancer in Florida.* Harmful Algae, 2002. 1(2): p. 157-168.
4. Bury, N., *The toxicity of cyanobacteria (blue-green algae) to freshwater fish.* Comp. Biochem. Physiol. A, 2007. 146(4): p. S92-S93.
5. San Diego-McGlone, M.L. et al., *Eutrophic waters, algal bloom and fish kill in fish farming areas in Bolinao, Pangasinan, Philippines.* Mar. Poll. Bull., 2008. 57(6--12): p. 295-301.
6. Hylland, K. et al., *Interactions between Eutrophication and Contaminants. IV. Effects on Sediment-dwelling Organisms.* Mar. Poll. Bull., 1996. 33(1--6): p. 90-99.
7. Allen, M.B. and D.I. Arnon, *Studies on Nitrogen-Fixing Blue-Green Algae. I. Growth and Nitrogen Fixation by Anabaena Cylindrica Lemm.* Plant Physiol., 1955. 30(4): p. 366-372.
8. Dauta, A. et al., *Growth rate of four freshwater algae in relation to light and temperature.* Hydrobiologia, 1990. 207(1): p. 221-226.
9. Lang, N., J. Krupp, and A. Koller, *Morphological and Ultrastructural Changes in Vegetative Cells and Heterocysts of Anabaena Variabilis Grown with Fructose.* J. Bacteriol., 1987. 169(2): p. 920-923.
10. Postema, M. et al., *Ultrasound-induced gas release from contrast agent microbubbles.* IEEE Trans. Ultrason. Ferroelectr. Freq. Control, 2005. 52(6): p. 1035-1041.
11. Ferrier, M.D. et al., *The effects of barley straw (Hordeum vulgare) on the growth of freshwater algae.* Biores. Tech., 2005. 96(16): p. 1788-1795.
12. Hao, H. et al., *Cavitation mechanism in cyanobacterial growth inhibition by ultrasonic irradiation.* Colloids Surf. B, 2004. 33(3--4): p. 151-156.
13. Ma, B. et al., *Influence of ultrasonic field on Microcystins produced by bloom-forming algae.* Colloids Surf. B, 2005. 41(2--3): p. 197-201.
14. Tang, J. et al., *Growth inhibition of the cyanobacterium Spirulina (Arthrospira) platensis by 1.7\,MHz ultrasonic irradiation.* J. Appl. Phycol., 2003. 15(1): p. 37-43.
15. Zhang, G., P. Zhang, and M. Fan, *Ultrasound-enhanced coagulation for Microcystis Aeruginosa removal.* Ultrason. Sonochem., 2009. 16(3): p. 334-338.
16. Zhang, G. et al., *Ultrasonic damages on cyanobacterial photosynthesis.* Ultrason. Sonochem., 2006. 13(6): p. 501-505.
17. Zhang, G. et al., *Ultrasonic frequency effects on the removal of Microcystis Aeruginosa.* Ultrason. Sonochem., 2006. 13(5): p. 446-450.
18. Chen, B. et al., *Ultrasound effects on the antioxidative defense systems of Porphyridium cruentum.* Colloids Surf. B, 2008. 61(1): p. 88-92.
19. Postema, M., *Onderzoek naar de veilige toepassing van ultrageluid gebruikt om blauwalg te bestrijden*, 2007, The University of Hull.
20. NATO Undersea Research Centre, *Human Diver and Marine Mammal Risk Mitigation Rules and Procedures*, 2006, NURC-SP-2006-008.
21. Culture Collection of Algae and Protozoa, *Media Recipes*. Vol. EG:JM. 2007.
22. Postema, M. and G. Schmitz, *Ultrasonic bubbles in medicine: influence of the shell.* Ultrason. Sonochem., 2007. 14(4): p. 438-444.
23. Postema, M. et al., *Ultrasound-induced encapsulated microbubble phenomona.* Ultrasound Med. Biol., 2004. 30(6): p. 827-840.
24. Postema, M. and G. Schmitz, *Bubble dynamics involved in ultrasonic imaging.* Expert Rev. Mol. Diagn., 2006. 6(3): p. 493-502.
25. Gorce, J.-M., M. Arditi, and M. Schneider, *Influence of bubble size distribution on the echogenicity of ultrasound contrast agents: a study of SonoVue™.* Invest. Radiol., 2000. 35(11): p. 661-671.

26. Sboros, V., *Response of contrast agent to ultrasound.* Adv. Drug Deliv. Rev., 2008. 60: p. 1117-1136.
27. Kudo, N. et al., *Study of the mechanism of fragmentation of a microbubble exposed to ultrasound using a high-speed observation system.* J. Acoust. Soc. Am., 2000. 108(5Pt2): p. 2547.
28. Lindner, J.R. and S. Kaul, *Delivery of drugs with ultrasound.* Echocardiography, 2001. 18(4): p. 329-337.
29. Postema, M. and O.H. Gilja, *Ultrasound-directed drug delivery.* Curr. Pharm. Biotechnol., 2007. 8(6): p. 355-361.
30. Dayton, P.A., J.S. Allen, and K.W. Ferrara, *The magnitude of radiation force on ultrasound contrast agents.* J. Acoust. Soc. Am., 2002. 112(5): p. 2183-2192.
31. Dayton, P.A. et al., *A preliminary evaluation of the effects of primary and secondary radiation forces on acoustic contrast agents.* IEEE Trans. Ultrason. Ferroelectr. Freq. Control, 1997. 44(6): p. 1264-1277.
32. Crum, L.A., *Bjerknes forces on bubbles in a stationary sound field.* J. Acoust. Soc. Am., 1975. 57(6): p. 1363-1370.
33. Tortoli, P. et al., *On the interaction between ultrasound and contrast agents during Doppler investigations.* Ultrasound Med. Biol., 2001. 27(9): p. 1265-1273.
34. Medwin, H., *Counting bubbles acoustically: a review.* Ultrasonics, 1977. 15: p. 7-13.
35. Di Marco, P., W. Grassi, and G. Memoli, *Experimental study on rising velocity of nitrogen bubbles in FC-72.* Int. J. Therm. Sci., 2003. 42: p. 435-446.
36. Leighton, T.G., *The Acoustic Bubble*1994, London: Academic Press.
37. de Jong, N., R. Cornet, and C.T. Lancée, *Higher harmonics of vibrating gas-filled microspheres. Part one: simulations.* Ultrasonics, 1994. 32(6): p. 447-453.
38. Duineveld, P.C., *Bouncing and coalescence phenomena of two bubbles in water*, in *Bubble Dynamics and Interface Phenomena*, J.R. Blake, J.M. Boulton-Stone, and N.H. Thomas, Editors. 1994, Kluwer Academic Publishers: Dordrecht. p. 447-456.
39. Postema, M. et al., *Ultrasound-induced microbubble coalescence.* Ultrasound Med. Biol., 2004. 30(10): p. 1337-1344.
40. Postema, M., M. Mleczko, and G. Schmitz, *Mutual attraction of oscilating microbubbles*, in *Advances in Medical Engineering*, T.M. Buzug et al., Editors. 2007, Springer: Berlin. p. 75-80.
41. Postema, M. et al., *High-speed photography during ultrasound illustrates potential therapeutic applications of microbubbles.* Med. Phys., 2005. 32(12): p. 3707-3711.
42. Prentice, P. et al., *Membrane disruption by optically controlled microbubble cavitation.* Nature Phys., 2005. 1: p. 107-110.
43. Bao, S., B.D. Thrall, and D.L. Miller, *Transfection of a reporter plasmid into cultured cells by sonoporation in vitro.* Ultrasound Med. Biol., 1997. 23: p. 953-959.
44. Chen, S. et al., *Optimization of ultrasound parameters for cardiac gene delivery of adenoviral or plasmid deoxyribonucleic acid by ultrasound-targeted microbubble destruction.* J. Am. Coll. Cardiol., 2003. 42(2): p. 301-308.
45. Greenleaf, W.J. et al., *Artificial cavitation nuclei significantly enhance acoustically induced cell transfection.* Ultrasound Med. Biol., 1998. 24(4): p. 587-595.
46. Kondo, I. et al., *Treatment of acute myocardial infarction by hepatocyte growth factor gene transfer: the first demonstration of myocardial transfer of a ``functional'' gene using ultrasonic microbubble destruction.* J. Am. Coll. Cardiol., 2004. 44(3): p. 644-653.
47. Kudo, N., K. Okada, and K. Yamamoto, *Sonoporation by single-shot pulsed ultrasound with microbubbles adjacent to cells.* Biophys. J., 2009. 96(12): p. 4866-4876.
48. Tachibana, K. et al., *Induction of cell-membrane porosity by ultrasound.* Lancet, 1999. 353: p. 1409.
49. Tinkov, S. et al., *Microbubbles as ultrasound triggered drug carriers.* J. Pharm. Sci., 2009. 98(6): p. 1935-1961.
50. Deng, C.X. and F.L. Lizzi, *A review of physical phenomena associated with ultrasonic contrast agents and illustrative clinical applications.* Ultrasound Med. Biol., 2002. 28(3): p. 277-286.

51. Klibanov, A.L., *Targeted delivery of gas-filled microspheres, contrast agents for ultrasound imaging.* Adv. Drug Deliv. Rev., 1999. 37: p. 139-157.
52. Postema, M. et al., *Nitric oxide delivery by ultrasonic cracking: some limitations.* Ultrasonics, 2006. 44(S1): p. e109-e113.
53. Shortencarier, M.J. et al., *A method for radiation-force localized drug delivery using gas-filled lipospheres.* IEEE Trans. Ultrason. Ferroelectr. Freq. Control, 2004. 51(7): p. 822-831.
54. Postema, M. et al., *Generation of a droplet inside a microbubble with the aid of an ultrasound contrast agent: first result.* Lett. Drug Des. Discov., 2007. 4(1): p. 74-77.
55. Voigt, J.-U., *Ultrasound molecular imaging.* Methods, 2009. 48: p. 92-97.
56. Philipp, A. and W. Lauterborn, *Cavitation erosion by single laser-produced bubbles.* J. Fluid Mech., 1998. 361: p. 75-116.
57. Kodama, T. and K. Takayama, *Dynamic behavior of bubbles during extracorporeal shock-wave lithotripsy.* Ultrasound Med. Biol., 1998. 24(5): p. 723-738.
58. Caskey, C.F. et al., *Microbubble tunneling in gel phantoms.* J. Acoust. Soc. Am., 2009. 125(5): p. EL183-EL189.
59. Kotopoulis, S. and M. Postema, *Microfoam formation in a capillary.* Ultrasonics, 2010. 50: p. 260-268.
60. Postema, M., O.H. Gilja, and A. van Wamel, *CEUS and sonoporation*, in *Fundamentals of Medical Ultrasonics*, M. Postema, Editor 2011, Spon press: London. p. 205-217.
61. van Wamel, A. et al., *Vibrating microbubbles poking individual cells: drug transfer into cells via sonoporation.* J. Control. Release, 2006. 112(2): p. 149-155.
62. Postema, M. and O.H. Gilja, *Jetting does not cause sonoporation.* Biomed. Eng., 2010. 55: p. S19-S20.
63. Marmottant, P. and S. Hilgenfeldt, *Controlled vesicle deformation and lysis by single oscillating bubbles.* Nature, 2003. 423: p. 153-156.
64. Delalande, A. et al., *Ultrasound-assisted microbubbles gene transfer in tendons for gene therapy.* Ultrasonics, 2009. 50: p. 269-272.
65. Kaddur, K. et al., *Transient transmembrane release of green fluorescent proteins with sonoporation.* IEEE Trans. Ultrason. Ferroelectr. Freq. Control, 2010. 57(7): p. 1558-1567.
66. Kotopoulis, S. et al., *Lithium niobate ultrasound transducers for MRI-guided ultrasonic microsurgery.* IEEE Trans. Ultrason. Ferroelectr. Freq. Control, 2011. 58(8): p. 1570-1576.
67. Livanec, P.W. and R.C. Dunn, *Single-molecule probes of lipid membrane structure.* Langmuir, 2008. 24(24): p. 14066-14073.
68. Postema, M. et al., *Simulations and measurements of optical images of insonified ultrasound contrast microbubbles.* IEEE Trans. Ultrason. Ferroelectr. Freq. Control, 2003. 50(5): p. 523-536.
69. Ehrenberg, B. et al., *Membrane potential can be determined in individual cells from the nernstain distribution of cationic dyes.* Biophys. J., 1988. 53: p. 785-794.
70. Takahashi, A., H. Yamaguchi, and H. Miyamoto, *Change in K+ current of HeLa cells with progression of the cell cycle studied by patch-clamp technique.* Am. J. Physiol., 1993. 265(2): p. C328-C336.
71. Krasovitski, B. et al., *Subcellular sonophores: ultrasound induced intramembrane cavitation.* Proc. Nat. Acad. Sci., 2011. 108(8): p. 3258-3263.

* Based on: Kotopoulis S, Schommartz A, Postema M. Sonic cracking of blue-green algae. Appl Acoust 2009 70(10):1306–1312; and Kotopoulis S, Schommartz A, Postema M. Safety radius for algae eradication at 200 kHz–2.5MHz. Proc IEEE Ultrason Symp 2008 1706–1709; and Kotopoulis S, Postema M. Microfoam formation in a capillary. Ultrasonics 2010 50(2):260–268; and Kotopoulis S, Postema M. Forming morphing microfoam. Proc Int Congr Acoust 2010 #25; and Delalande A, Kotopoulis S, Rovers T, Pichon C, Postema M. Sonoporation at a low mechanical index. Bub Sci Eng Tech 2011 3(1):3-11.